Concurrent Decadal Mesoscale Eddy Modulations in the Western North Pacific Subtropical Gyre

BO QIU AND SHUIMING CHEN

Department of Oceanography, University of Hawaii at Manoa, Honolulu, Hawaii

(Manuscript received 25 July 2012, in final form 11 September 2012)

ABSTRACT

Satellite altimeter data of the past two decades are used to investigate the low-frequency mesoscale eddy variability inside the western North Pacific subtropical gyre. Eddy activity modulations with a decadal time scale are detected concurrently within the 18°–28°N band, including the three branches of the Subtropical Countercurrent (STCC) and the Hawaiian Lee Countercurrent (HLCC). Lagging behind the Pacific decadal oscillation (PDO) index by six months, enhanced eddy activities were detected in 1995–98 and 2003–06, whereas the eddy activities were below the average in 1999–2002 and 2009–11. Analysis of the temperature and salinity data that became available after 2001 via the International Argo Program reveals that the modulating eddy activities are due to the decadal change in the upper-ocean eastward shear in the broad-scale STCC–HLCC band. By conducting an upper-ocean temperature budget analysis, the authors found that this observed eastward shear change can be effectively accounted for by the decadal-varying surface heat flux forcing. Using the Argo-based temperature and salinity data, it is further found that the decadal subsurface potential vorticity (PV) signals to the north and beneath the STCC–HLCC were vertically coherent and *not* confined to the mode water isopycnals. Adjusting to the PDO-related surface forcing, these subsurface PV anomalies lagged behind the upper-ocean eastward shear signals and likely made minor contributions to generate the decadal-varying eddy signals observed in the western North Pacific subtropical gyre.

1. Introduction

Two well-defined zonal bands of elevated mesoscale eddy variability exist in the extratropical North Pacific Ocean (Fig. 1). The first band follows the path of the Kuroshio and Kuroshio Extension (KE) east and southeast of Japan along approximately 35°N. Eddy variability along this zonal band is dominated by decadal fluctuations that have been the subject of interest to many recent data analysis and modeling studies (e.g., Qiu and Chen 2005, 2011; Taguchi et al. 2007; Ceballos et al. 2009; Nakano and Ishikawa 2010). The consensus from these studies is that the level of mesoscale eddies in this band depends on the dynamic state of the KE and is controlled by the basin-scale surface wind stress curl forcing over the eastern North Pacific Ocean. Specifically, when the eastern anomalous wind stress curl forcing is positive during the positive Pacific decadal oscillation (PDO; Mantua et al. 1997) phase, the level of mesoscale eddies tends to be enhanced nonlinearly after the wind-induced, lowered sea surface height (SSH) signals propagate westward into the KE region with a delay of ~4 years. The reverse is true in the negative PDO phase when the anomalous wind stress curl forcing switches to negative over the eastern North Pacific Ocean. For comprehensive review articles on the KE eddy variability and its impact, readers are referred to Qiu (2002), Kelly et al. (2010), and Oka and Qiu (2012).

The second zonal band with elevated mesoscale eddy variability is located within the southern half of the wind-driven subtropical gyre of the western North Pacific between 18° and 28°N. Although the Sverdrup theory predicts a *westward* barotropic interior flow within this band (see, for example, Fig. 4 in Huang and Qiu 1994), an *eastward* shear of zonal flows appears in the upper ocean of this band (Fig. 2a). In fact, though weak in magnitude, the near-surface flows inside much of this band are directed *eastward* and these eastward flows are commonly referred to as Subtropical Countercurrent (STCC; see Fig. 2b). The STCC owes its existence to the combined forcing of surface wind stresses and heat

Corresponding author address: Dr. Bo Qiu, Department of Oceanography, University of Hawaii at Manoa, 1000 Pope Road, Honolulu, HI 96822.
E-mail: bo@soest.hawaii.edu

DOI: 10.1175/JPO-D-12-0133.1

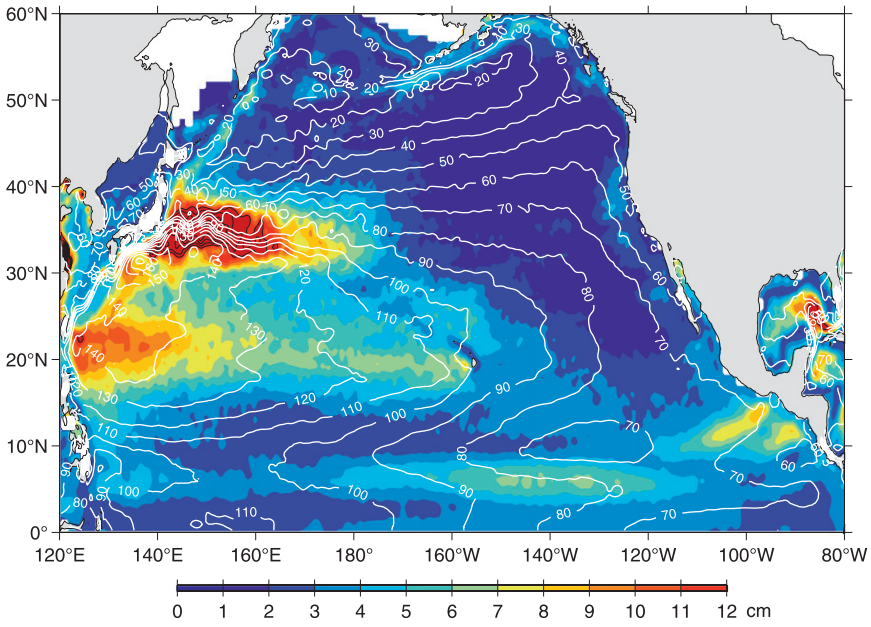

FIG. 1. Root-mean-squared sea surface height variability (colors) in the North Pacific based on high-pass-filtered satellite altimeter data from October 1992 to June 2012. The high-pass filter has a half-power at 180 days. Regions where the rms SSH variability > 12 cm are indicated by thin black contours (with a contour interval at 2 cm). White contours denote the mean SSH (cm) field by Rio et al. (2011).

fluxes and a recent article by Kobashi and Kubokawa (2012) provided an up-to-date review on the mechanisms for the STCC's generation in the wind-driven subtropical gyre of the North Pacific Ocean. Though Fig. 2a indicates the presence of broad-scale eastward shears within the 18°–28°N band, the time-mean STCC is comprised of three, quasi-stationary, eastward jets: the southern STCC centered along ~19.5°N from 125°E to 180°, the northern STCC along ~24°N from 125°E to 180°, and the eastern STCC north of the Hawaiian Islands along ~25°N from 180° to 150°W (Kobashi et al. 2006). In addition to these quasi-stationary STCC jets, the Hawaiian Lee Countercurrent (HLCC), located west of the Hawaii Island along 19.5°N, is another well-anchored eastward jet that contributes to the broad-scale eastward shears appearing in the interior of the North Pacific subtropical gyre (e.g., Qiu et al. 1997; Flament et al. 1998; Xie et al. 2001; Yoshida et al. 2011).

Dynamically, the near-surface eastward-flowing STCCs and HLCC result in the meridional potential vorticity (PV) gradient in the upper 200 m ocean to be positive. Below this upper layer exists the wind-driven, westward-flowing, North Equatorial Current (NEC; Fig. 2b). With the permanent thermocline associated with the NEC deepening toward north, the meridional PV gradient in the subsurface layer at ~(200–800) m is negative. This reversal in sign of the meridional PV gradients results in baroclinic instability and is the energy source for the elevated eddy variability detected along the 18°–28°N band in the western North Pacific Ocean (Qiu 1999; Roemmich and Gilson 2001; Kobashi and Kawamura 2002).

As indicated in Fig. 2b, the surface-trapped vertical shear associated with the STCC and NEC between 18° and 28°N is very different in nature from the deep-reaching KE jet along ~35°N. It is not surprising, as a result, that the eddy signals within these two zonal bands in the North Pacific Ocean exhibit different characteristics. For example, the eddy kinetic energy (EKE) level in the STCC band has a well-defined annual cycle with a maximum in April–May and a minimum in December–January. This annual cycle in EKE level is due to the seasonal changes in the STCC's intensity that determines the growth rate of baroclinic instability (Qiu 1999; Kobashi and Kawamura 2002; Noh et al. 2007). Seasonal eddy modulations are largely absent in the KE band.

Compared to the KE band in the North Pacific Ocean, the eddy variability on the interannual and longer time scales is less systematically explored for the STCC band. By combining repeat hydrographic data along 137°E and the satellite altimeter data, Qiu and Chen (2010) explored the interannual EKE signals in the northern–southern STCC band. They found that the eastward

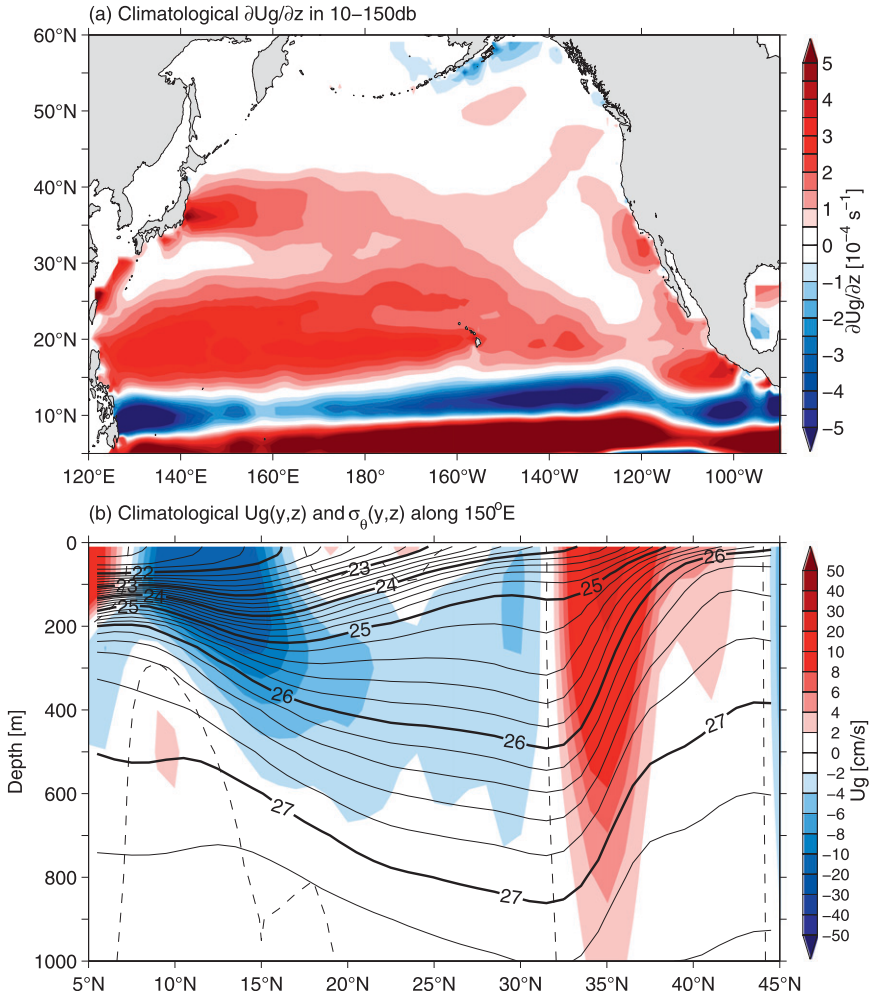

FIG. 2. (a) Vertical shear of the zonal geostrophic velocity $\partial U_g/\partial z$ averaged in the 10–150-m upper ocean. (b) Cross-section profiles of density (contours) and mean zonal geostrophic velocity (colors) along 150°E. Both plots are based on the climatological MOAA–GPV *T*–*S* data. The reference level for U_g is 2000 dbar.

shear of the eastward-flowing STCC was stronger in eddy-rich years than in eddy-weak years and they emphasized the wind-induced Ekman convergence forcing in causing the interannual changes in the eastward shear of the STCC. The importance of the meridional Ekman convergence forcing in controlling the interannual modulations in the late winter northern STCC was also stressed by Kobashi and Xie (2012). For both the eastern STCC and the HLCC, Chen and Qiu (2010) and Yoshida et al. (2011) have found that the EKE level in their respectively studied region is positively correlated with the PDO index. In particular, Yoshida et al. (2011) found that the latitude-dependent surface heat flux forcing played a more crucial role than the Ekman convergence forcing in controlling the decadal-varying eastward shear of the HLCC. Rather than the surface forcing, Sasaki et al. (2012) have attributed the interannual changes in the HLCC's intensity to the anomalous southward intrusion of central mode water and eastern subtropical mode water.

With the high-precision satellite altimeter measurements now accumulated over a two-decade period, we attempt in this study to reexamine the low-frequency mesoscale eddy signals in the North Pacific STCC band. Specific questions to be addressed include the following. Are the mesoscale eddy signals similarly modulated in time in the three STCC and the HLCC bands? Are these modulating eddy signals accompanied by corresponding changes in the upper ocean eastward shear? To what extent can the surface wind stress and heat flux forcing account for the observed eastward shear changes? Is there observational evidence for the time-varying mode

water signals originating in the KE latitude to extend equatorward beneath the STCC and HLCC? If yes, are they responsible for the low-frequency eastward shear changes detected along the STCC–HLCC bands?

One important dataset that has not been fully utilized in the previous studies of the STCC–HLCC is the profiling temperature and salinity data from the International Argo Program (Roemmich et al. 2009). Although reliable data coverage for the World Ocean has only been available for the past 10 years, this new data source, as will be demonstrated in this study, provides us with the indispensable subsurface information for understanding the decadally modulating STCC–HLCC system and answering the above-listed questions.

2. Decadal eddy modulations from altimeter measurements

To examine the mesoscale eddy changes in the subtropical gyre interior, we use the global SSH anomaly dataset compiled by the Collecte Localisation Satellites (CLS) Space Oceanographic Division of Toulouse, France. This dataset merges along-track SSH measurements from all satellite altimeter missions after October 1992 and has a 7-day temporal resolution and a 1/3°-longitude Mercator spatial resolution (Ducet et al. 2000). The data period analyzed in this study extends from October 1992 to June 2012.

An effective way to capture the low-frequency eddy variability in the broad subtropical gyre is to conduct an empirical orthogonal function (EOF) analysis of the eddy kinetic energy field, where eddy kinetic energy is calculated using the SSH anomaly data h' based on geostrophy:

$$\mathrm{EKE} = \frac{1}{2}\left[\left(\frac{g}{f}\frac{\partial h'}{\partial x}\right)^2 + \left(\frac{g}{f}\frac{\partial h'}{\partial y}\right)^2\right], \qquad (1)$$

where g is the gravity constant and f the Coriolis parameter. To exclude influences of the eddy signals from the tropical and Kuroshio–Kuroshio Extension regions, the EOF analysis is performed inside the domain from 10° to 30°N and from 125°E to 110°W. Figure 3a shows the spatial pattern of the first EOF mode during our analysis period. It has a pattern geographically similar to that captured in the rms SSH map of Fig. 1; specifically, the high eddy signals are centered along ~20°N west of the Hawaiian Islands and tend to increase progressively in amplitude and meridional width toward the west. In addition, a localized enhanced eddy variability area is also seen to the north of the Hawaiian Islands around 22°–28°N and 170°–150°W, corresponding to eastern

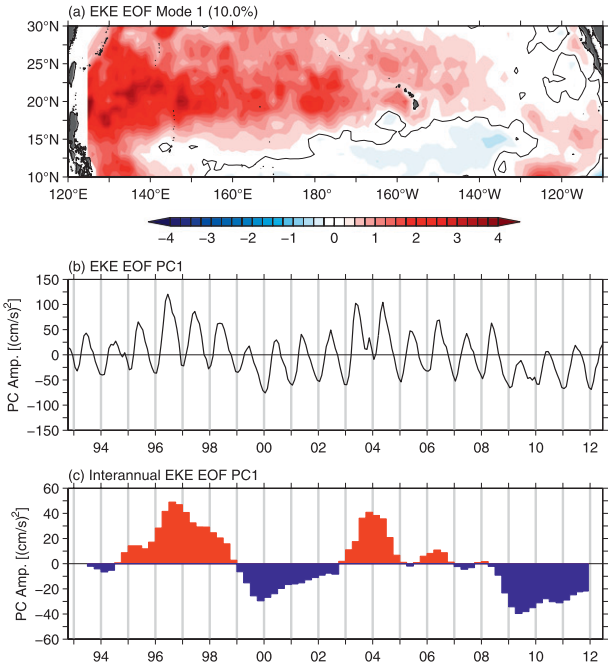

FIG. 3. First EOF mode of the SSH-derived eddy kinetic energy in the subtropical North Pacific Ocean: (a) spatial pattern and (b) corresponding weighting function. The mode explains 10.0% of the total EKE variance and black lines in (a) indicate zero amplitude contours. (c) Interannual changes of the weighting function after a 1-yr running-mean average is applied to (b).

STCC band. The corresponding weighting coefficient of the first EOF mode is shown in Fig. 3b. In accordance with the previous analyses (Qiu 1999; Kobashi and Kawamura 2002; Noh et al. 2007; Yoshida et al. 2011), the eddy signals have a well-defined annual cycle with a maximum in spring and a minimum in winter. This annual EKE modulation, as we noted in the introduction, is due to the seasonal changes in eastward shear between the surface STCC–HLCC and the subsurface NEC that controls the intensity of baroclinic instability.

By removing the annual running-mean signals from Fig. 3b and averaging seasonally, Fig. 3c reveals that the EKE time series in the subtropical gyre interior modulates quasi-regularly on the decadal time scales: higher than normal EKE signals are observed in 1995–98 and 2003–06, whereas lower than normal EKE signals are detected in 1999–2002 and 2009–11. It is worth emphasizing that the decadal EKE signals in Fig. 3c have a peak-to-peak amplitude of 200~300 $\mathrm{cm^2\ s^{-2}}$, which is on par with the amplitude of the *mean* annual EKE signals. For brevity, we will hereafter refer to the low-pass-filtered EKE time series of Fig. 3c as the decadal EKE index in the STCC band.

To further clarify the spatial characteristics of the decadal EKE signals, we present in Fig. 4 the EKE

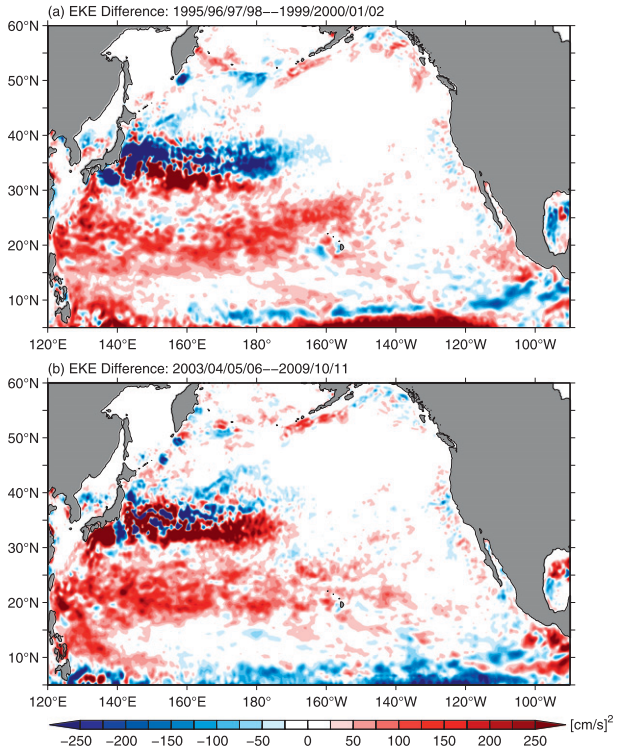

FIG. 4. Difference in EKE level in the North Pacific Ocean: (a) years (1995–98) − (1999–2002) and (b) (2003–06) − (2009–11).

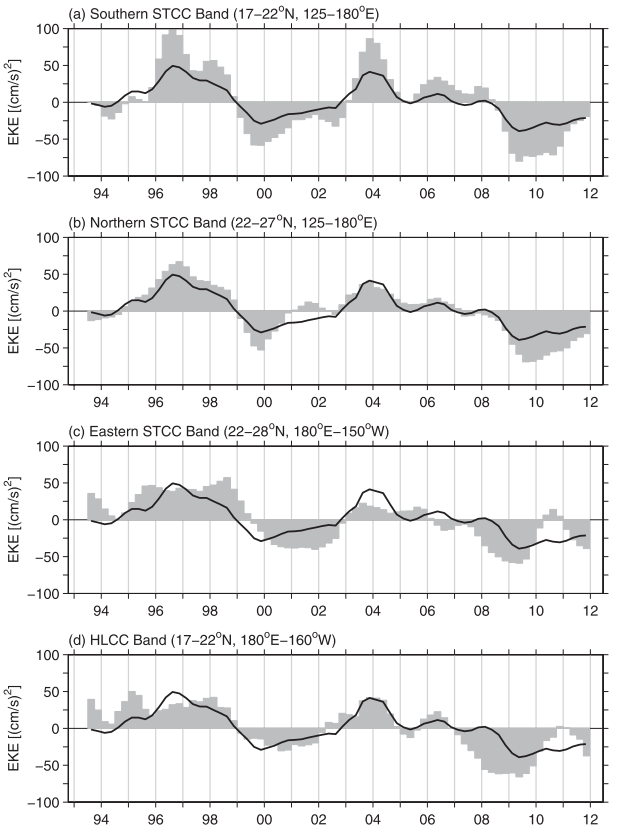

FIG. 5. Low-pass-filtered EKE time series (gray shading) averaged in the band of (a) southern STCC (17°–22°N, 125°–180°E), (b) northern STCC (22°–27°N, 125°–180°E), (c) eastern STCC (22°–28°N, 180°E–150°W), and (d) HLCC (17°–22°N, 180°E–160°W). Black lines indicate the decadal STCC EKE index derived from the first EOF mode (i.e., Fig. 3c).

difference maps of 1995–98 minus 1999–2002 (Fig. 4a) versus 2003–06 minus 2009–11 (Fig. 4b). In both maps of eddy-rich minus eddy-weak phases, the differential EKE signals in the 10°–30°N band of our interest exhibit a similar geographical pattern, suggesting the repetitive nature of the EKE signals detected within the broad STCC band. In contrast, outside of the 10°–30°N band, the differential EKE signals lack the coherent signs between the two maps. For example, along the Kuroshio Extension north of 31°N, the differential EKE values are largely positive in Fig. 4b, whereas negative values appear more dominant in Fig. 4a.

In concluding this section, it is instructive to compare the EKE time series averaged independently within the three STCC and the HLCC bands (see Fig. 5). To focus on the low-frequency variability, seasonal signals have been removed with the application of an annual running-mean filter. The black lines in Fig. 5 show the decadal EKE index based on the first EOF mode. Owing to their large variance (recall Fig. 3a), the EKE time series in the northern and southern STCC bands agree favorably with the EOF-based decadal EKE index. The linear correlation coefficients between the EKE time series and index are 0.96 in Fig. 5a and 0.94 in Fig. 5b, respectively. The EKE time series in the eastern STCC and the HLCC bands, on the other hand, share many detailed temporal features between the two subregions (cf. Figs. 5c and 5d). Though less well correlated to the EOF-based decadal EKE index than those of the northern–southern STCCs, their decadal-varying signals are, nevertheless, reasonably represented by the STCC's decadal EKE index (the linear correlation coefficients in Figs. 5c and 5d are 0.73 and 0.77, respectively). In other words, the mesoscale EKE signals are largely modulated in a coherent fashion among the four eastward-flowing surface jets in the subtropical gyre interior of the North Pacific Ocean.

3. Decadal subsurface ocean variability in the subtropical gyre interior

To clarify the cause underlying the decadal EKE signals identified along the STCC band, it is helpful to examine the circulation changes in the subtropical gyre interior in terms of zonal velocity shear. To do so, we utilize the monthly temperature and salinity dataset

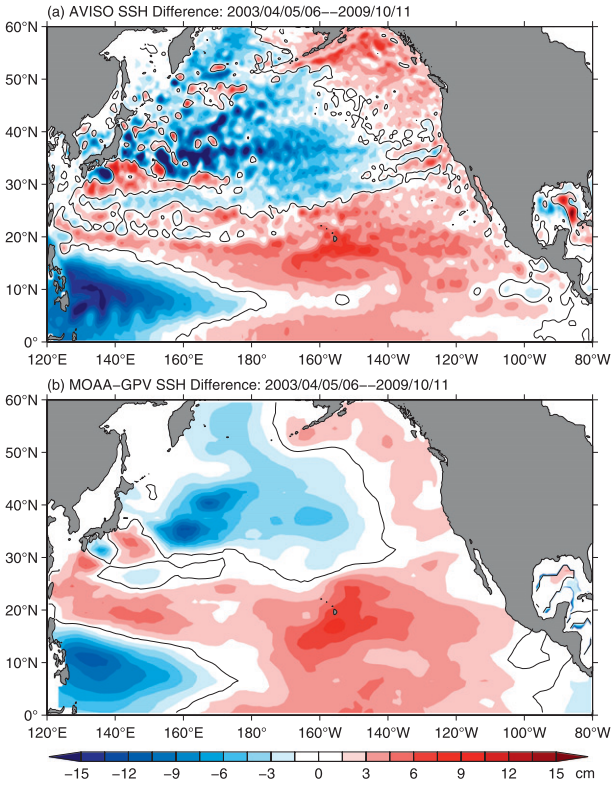

FIG. 6. Difference in sea surface height (cm) for years (2003–06) − (2009–11) derived from (a) the Archiving, Validation, and Interpretation of Satellite Oceanographic data (AVISO) SSH dataset and (b) the MOAA–GPV dataset of Hosoda et al. (2008).

compiled by Hosoda et al. (2008) that combines quality-controlled Argo-profiling data and other available moored and ship observations. This dataset is known as the monthly objective analysis using the Argo data (MOAA)–grid point value (GPV) and has a 1° spatial resolution for the 2000-m upper ocean. As the MOAA–GPV dataset became available in 2001 following the start of the international Argo project, the focus of our following analyses is on the recent decadal change in EKE between 2003–06 and 2009–11.

To evaluate the validity of the MOAA–GPV dataset, we first compare the SSH difference between 2003–06 and 2009–11 derived from the MOAA–GPV temperature–salinity data (Fig. 6b) against that measured by satellite altimeters (Fig. 6a). Although it fails to recover the small-scale SSH features evident in Fig. 6a, the MOAA–GPV dataset is able to capture faithfully the broad-scale features that appear in the 18°–28°N band of our interest. These include the overall positive (negative) differential SSH anomalies in the southern (northern) half of the band west of 160°E and the positive differential SSH anomaly located to the southeast of the Hawaiian Islands. Dynamically, these differential SSH features imply an increased surface eastward shear in 2003–06 as compared to 2009–11 in the 18°–28°N band.

To investigate how this increased eastward shear changes with depth, we regress the time-varying $\partial U_g/\partial z$ signals inferred from the MOAA–GPV data against the decadal EKE index shown in Fig. 3c. Figure 7b shows the regressed $\partial U_g/\partial z$ value averaged inside 18°–28°N and 125°E–150°W as a function of depth. It reveals that the enhanced eastward shear during the eddy-rich years (i.e., 2003–06) is confined to the upper ocean of ~300 m. Below the 300-m depth, the regressed $\partial U_g/\partial z$ value becomes negative. As the mean zonal geostrophic flow U_g below the 300-m depth in the region is negative (see Fig. 7a), this negative value implies a weak enhancement of the westward-flowing NEC during 2003–06 as compared to 2009–11.

To further clarify the spatial pattern of the decadal eastward shear signals shown in Fig. 7b, we plot in Fig. 8 the differential $\partial U_g/\partial z$ values in the upper 150 m ocean between 2003–06 and 2009–11 (the upper 150-m layer is selected here because it is where the mean $\partial U_g/\partial z$ is largest; choosing a deeper layer does not change the pattern shown in Fig. 8 qualitatively). Within the southern subtropical gyre of our interest from 18°N to 28°N, the differential $\partial U_g/\partial z$ has spatially coherent positive values, signaling the broad-scale nature of the decadal eastward shear changes that lie behind the in-phase EKE signals within the entire STCC band of the western North Pacific Ocean. Using the same MOAA–GPV dataset, Sasaki et al. (2012) have recently emphasized the strengthening of the eastward-flowing HLCC in 2003 and 2005. The result of Fig. 8 suggests that this strengthening in the upper-ocean eastward shear in 2003–06 is not restricted to the HLCC band but is a spatially coherent feature with a broader scale. As will be discussed in section 5, recognition of this broad-scale coherent change in $\partial U_g/\partial z$ is important in unraveling the dynamic causes behind the decadal EKE signals detected in this study.

4. Decadal surface wind and buoyancy forcings

Both the surface wind and buoyancy forcing can exert an impact upon the eastward shear in the upper ocean (e.g., Roden 1975; Kazmin and Rienecker 1996; Nakamura and Kazmin 2003). The specific question to be addressed in this section is to what extent the observed $\partial U_g/\partial z$ changes shown in Fig. 8 can be explained *quantitatively* by the time-varying surface wind and heat flux forcings. To answer this question, we note first that the depth-averaged $\partial U_g/\partial z$ can be related to the meridional temperature gradient via the thermal wind balance where $\langle\cdot\rangle$ indicates depth averaging

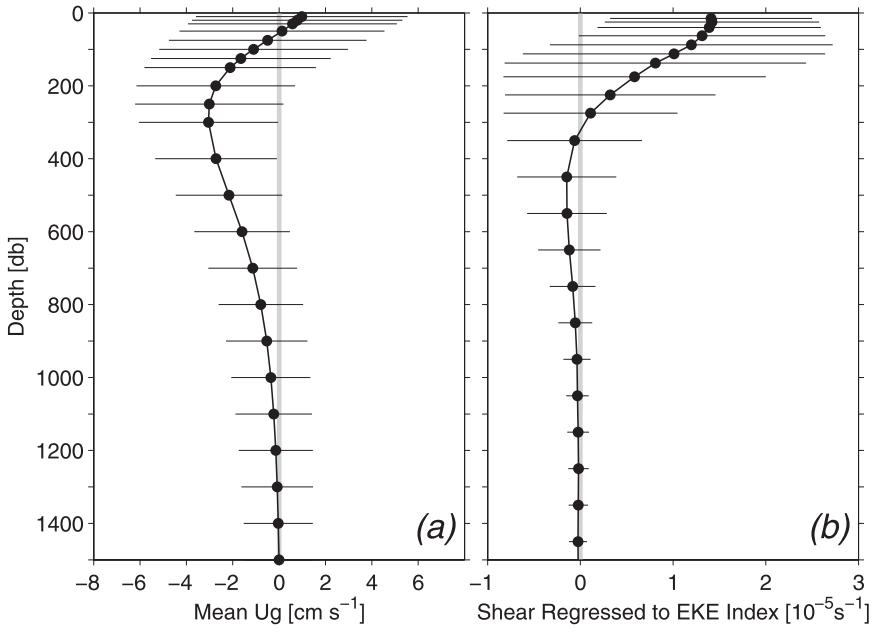

FIG. 7. (a) Mean zonal geostrophic velocity U_g averaged in 18°–28°N and 125°E–150°W as a function of depth. (b) Time-varying $\partial U_g/\partial z$ averaged in the 18°–28°N and 125°E–150°W box regressed to the EKE index of Fig. 3c. Both plots are based on the monthly MOAA-GPV T–S data and horizontal bars indicate standard deviations. The reference level for U_g is 2000 dbar.

$$\left\langle \frac{\partial U_g}{\partial z} \right\rangle = -\frac{\alpha g}{f}\frac{\partial \langle T \rangle}{\partial y}, \tag{2}$$

where T is the water temperature, α is the thermal expansion coefficient, and denoted is the depth average in the surface layer $H_0 = 150$ m. In writing Eq. (2), we have assumed that the density signal in our study is given by $\rho = \rho_0[1 - \alpha(T - T_0)]$, where ρ_0 and T_0 are the reference density and temperature, respectively. A temperature budget equation in the surface 150 m can be written as:

$$\frac{\partial \langle T \rangle}{\partial t} = -\langle \mathbf{u}_{\mathrm{Ek}} \rangle \cdot \nabla \langle T \rangle + \frac{Q_{\mathrm{net}}}{\rho_0 c_p H_0} + \text{other terms}, \tag{3}$$

where $\langle \mathbf{u}_{\mathrm{Ek}} \rangle$ is the depth-averaged Ekman flux in the upper 150-m layer and is related to the surface wind stress vector $\boldsymbol{\tau}$ by $\mathbf{k} \times \langle \mathbf{u}_{\mathrm{Ek}} \rangle = \boldsymbol{\tau}/\rho_0 f H_0$.[1] In (3), Q_{net} is the net surface heat flux (positive into the ocean), c_p is the specific heat of seawater, and "other terms" denote the internal oceanic processes, such as geostrophic advection, vertical entrainment, and eddy diffusion.

By combining Eqs. (2) and (3), we have

$$\frac{\partial}{\partial t}\left(\left\langle \frac{\partial U_g}{\partial z} \right\rangle\right) = \frac{\alpha g}{f}\frac{\partial}{\partial y}(\langle \mathbf{u}_{\mathrm{Ek}} \rangle \cdot \nabla \langle T \rangle) - \frac{\alpha g}{f \rho_0 c_p H_0}\frac{\partial Q_{\mathrm{net}}}{\partial y} + \text{other terms}. \tag{4}$$

Dynamically, the first term on the rhs of Eq. (4) signifies the wind forcing through Ekman flux convergence and the second term, the surface heat flux forcing through y-dependent heating–cooling. Figure 9a shows the time

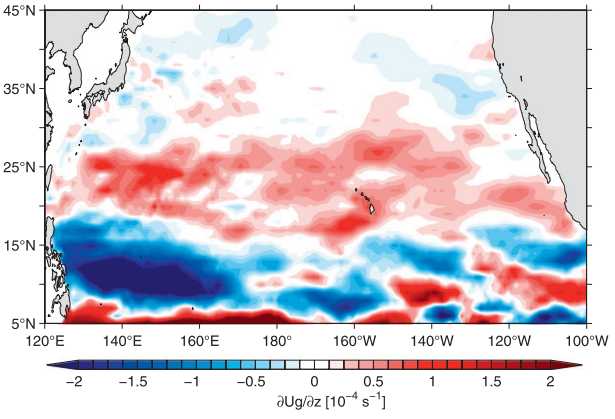

FIG. 8. Difference in $\partial U_g/\partial z$ in the 10–150-dbar upper ocean for years (2003–06) − (2009–11). Based on the monthly MOAA–PGV T–S data.

[1] Although the upper 150-m layer is chosen for the temperature budget analysis in this study, selecting a different layer thickness (e.g., $H_0 = 200$ m) does not alter the conclusions reached in this section.

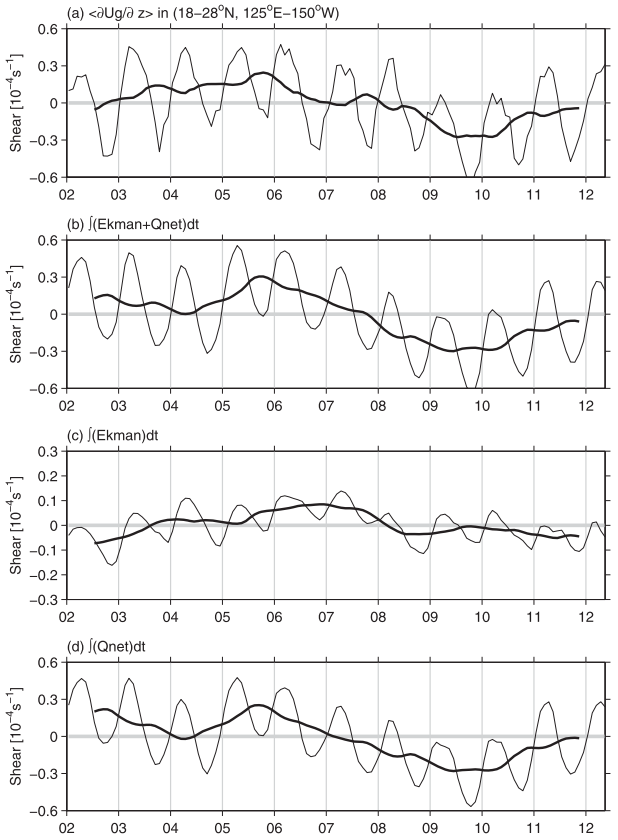

FIG. 9. (a) Time series of $\langle \partial U_g/\partial z \rangle$ averaged in the 18°–28°N and 125°E–150°W region based on the monthly MOAA-GPV dataset. (c) Time series of $(\alpha g/f)\int \partial(\langle \mathbf{u}_{\rm Ek} \rangle \cdot \nabla \langle T \rangle)/\partial y \, dt$, and (d) time series of $-(\alpha g/f\rho_0 c_p H_0)\int \partial Q_{\rm net}/\partial y \, dt$. (b) Sum of the two forcing terms given in (c) $\int$(Ekman) dt and (d) $\int(Q_{\rm net})\, dt$. In all plots, thin lines indicate the original monthly time series and thick lines the time series after the removal of annual running-mean values.

series of $\langle \partial U_g/\partial z \rangle$ averaged in the region of 18°–28°N and 125°E–150°W based on the monthly MOAA–GPV dataset. In Figs. 9c and 9d, we plot the time series of the time-integrated Ekman flux convergence forcing and the time-integrated surface heat flux forcing within the same 18°–28°N and 125°E–150°W region, respectively. In evaluating $\langle \mathbf{u}_{\rm Ek} \rangle$ and $Q_{\rm net}$, we have used the monthly wind stress and net surface heat flux data from the National Centers for Environmental Prediction (NCEP)–National Center for Atmospheric Analysis (NCAR) reanalysis (Kistler et al. 2001), and estimation for $\langle T \rangle$ is again based on the monthly MOAA–GPV dataset.

Figure 9b shows the sum of the two forcing time series. With the exception for 2004 (during which the summed forcing is relatively weak), the time series of Fig. 9b exhibits a decadal signal similar to that of $\langle \partial U_g/\partial z \rangle$ both in terms of phase and amplitude (cf. Fig. 9a). A look into Figs. 9c and 9d indicates that ~90% of this decadal signal in Fig. 9b comes from the surface heat flux forcing, with the contribution from the Ekman flux convergence forcing at only ~10% (note that the y axis in Fig. 9c has a different scale). This result is in agreement with the analysis by Yoshida et al. (2011) who found a similar dominance of the surface heat flux forcing in controlling the decadal eastward shear changes in the HLCC band of 17°–21.7°N and 170°E–160°W. From Fig. 9, it is also evident that the combined surface wind and heat flux forcing is capable of explaining the seasonal changes in $\langle \partial U_g/\partial z \rangle$ quantitatively. Like the decadal signals, the seasonal surface heat flux forcing again makes a greater contribution to the seasonal $\langle \partial U_g/\partial z \rangle$ signals, accounting for ~80% of their amplitude, than the seasonal Ekman flux convergence forcing. This seasonal forcing result is consistent with the findings reached previously by Kazmin and Rienecker (1996; their Fig. 3).

Although the Ekman flux convergence forcing plays a minor role in determining the eastward shear variability in the surface 150-m ocean, the surface wind fluctuations are crucial for the decadal changes in the intensity of the wind-driven subtropical gyre. To illustrate this, we plot in Fig. 10a the difference in surface wind stress vectors and Sverdrup transport streamfunction between 2003–06 and 2009–11 based on the NCEP–NCAR reanalysis wind stress data. Within the 18°–28°N band of our interest, there exists a clear intensification of the anticyclonic Sverdrup circulation during 2003–06 because of the overlying, increased negative wind stress curl. This regional spin up of the wind-driven anticyclonic gyre is supported by Fig. 10b in which we plot the geostrophic transport streamfunction difference between 2003–06 and 2009–11 based on the MOAA–GPV dataset. Here, the geostrophic transport is calculated for the upper 2000 m ocean. Further evidence for the decadal changes of the western North Pacific subtropical gyre responding to the overlying wind stress curl variability has been found in the observed Kuroshio transport in the East China Sea (Andres et al. 2009).

Notice that the strengthening of this wind-driven anticyclonic gyre is not only important for the increased SSH signals in the 18°–28°N band shown in Fig. 6, it also impacts the subsurface density structures through deepening of the permanent pycnocline. This point will be stressed in the next section in conjunction with the decadal PV signals in the interior ocean.

5. Decadal changes in the interior ocean PV field

With the STCC bordered beneath and to the north by the subtropical mode water (STMW) and central mode water (CMW) in the western North Pacific, it is relevant to ask if the decadal STCC changes detected in this study are induced by changes originating from these mode

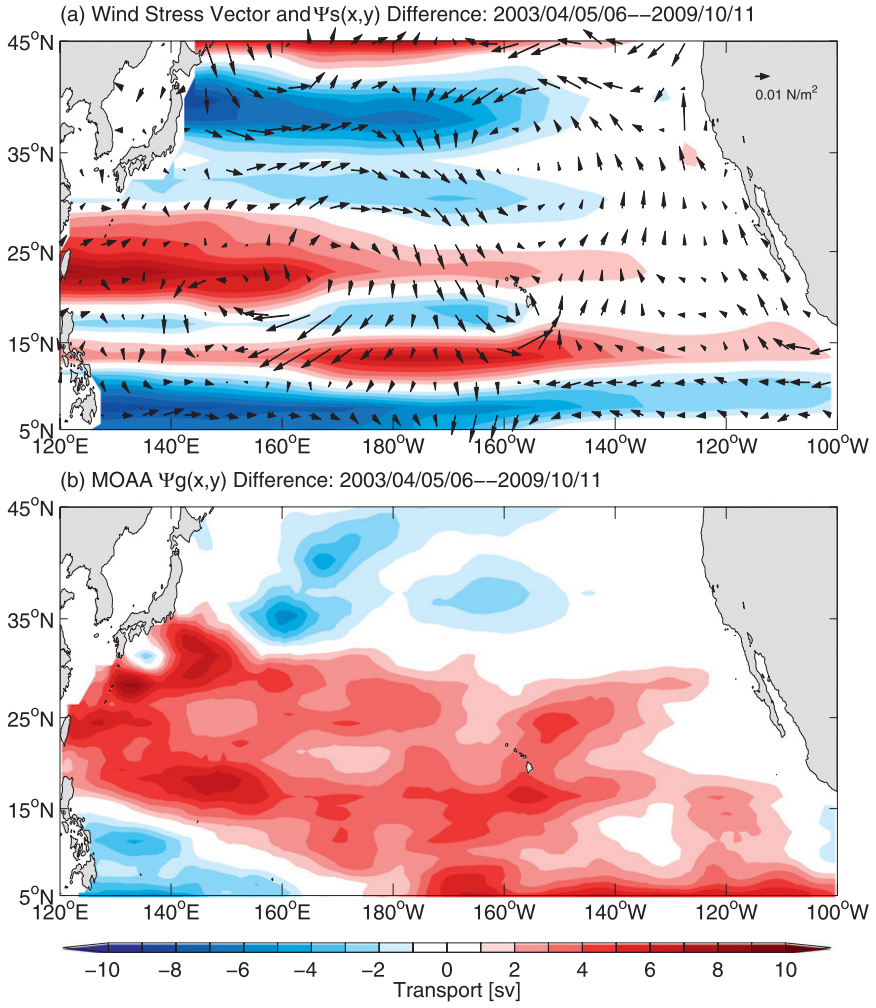

FIG. 10. (a) Difference in surface wind stress vectors and Sverdrup transport streamfunction Ψ_S (colors) for years (2003–06) − (2009–11). Here, $\Psi_S(x, y) = -(f/\beta\rho_0)\int_x^{x_e} \nabla \times \boldsymbol{\tau}\, dx$, where x_e is the eastern boundary with $\boldsymbol{\tau}$ given by the NCEP–NCAR reanalysis. (b) Difference in geostrophic transport streamfunction Ψ_g as in (a). Here, $\Psi_g(x, y) = -\rho_0\int_x^{x_e} V_g(x, y)\, dx$, where V_g is the meridional geostrophic transport of the upper 2000-m layer calculated from the MOAA–GPV dataset.

waters. To explore this issue, we utilize the MOAA–GPV dataset again and focus on the two density surfaces: (25.3–25.5) σ_θ and (25.9–26.1) σ_θ. Subduction of low-PV STMW along the (25.3–25.5) σ_θ surface is considered responsible for the northern–southern STCC formation, whereas subduction of low-PV CMW on the latter (25.9–26.1) σ_θ surface is thought to be important for the eastern STCC–HLCC formation (e.g., Kobashi et al. 2006; Yamanaka et al. 2008; Xie et al. 2011; Nonaka et al. 2012; Sasaki et al. 2012; Sugimoto et al. 2012).

Figures 11a and 11b show the differential PV values between 2003–06 and 2009–11 on the STMW and CMW isopycnal surfaces, respectively. Here, PV is evaluated by $-(f/\rho)\partial\sigma_\theta/\partial z$ using the MOAA–GPV data. On both of these isopycnal surfaces, the differential PV values are mostly negative within the western wind-driven subtropical gyre. With the along-isopycnal $\partial(\mathrm{PV})/\partial y < 0$, these maps are indicative of enhanced low-PV waters in 2003–06 possibly lifting up the upper-ocean isopycnal surfaces. Caution, however, needs to be exercised in inferring the causes behind the broad-scale differential PV signals in the STCC band of our interest. In Fig. 12a, we plot the PV anomalies averaged zonally from 125°E to 180° on the (25.3–25.5) σ_θ surface as a function of time and latitude. As indicated by the acceleration potential contours in Fig. 11a, 125°E–180° is the band within which subducted STMW signals are expected to expand equatorward into the subtropical gyre interior. Similarly, Fig. 13a shows the PV anomalies averaged zonally from 170°W to 140°W on the (25.9–26.1) σ_θ surface relevant to the CMW ventilation.

If the PV anomalies are assumed to start from the southern STMW and CMW latitude of ~30°N and be

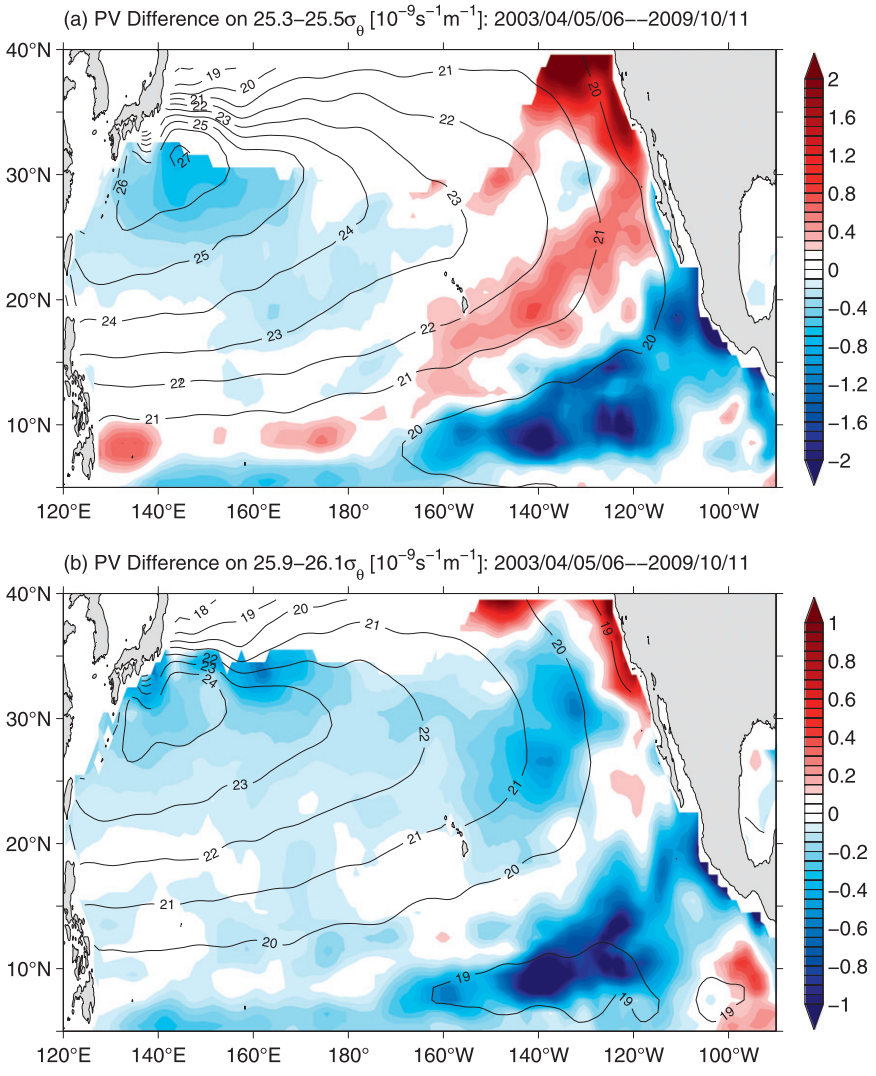

FIG. 11. As in Fig. 10, but for (potential vorticity on the (25.3–25.5) σ_θ surface of STMW. Black contours denote the acceleration potential field referenced to 2000 dbar. (b) As in (a), but for the (25.9–26.1) σ_θ surface of CMW.

carried equatorward by the gyre and eddy advection, it would take them more than 3.5 and 4.2 years to reach 18°N on the (25.3–25.5) σ_θ and (25.9–26.1) σ_θ surfaces, respectively.[2] The PV anomalies observed on the (25.3–25.5) σ_θ and (25.9–26.1) σ_θ surfaces in Figs. 12a and 13a appear to extend equatorward much faster than these predicted time intervals. In fact, the observed decadal PV anomalies on these two isopycnal surfaces emerge nearly concurrently in *all* latitudes within a period of <2 yr. This result implies that instead of originating in the STMW and CMW formation sites and being subducted thereafter on their respective isopycnal surfaces, the vertically-coherent PV anomalies in the STCC band are more likely to be generated by the decadal-varying wind stress curl forcing. Specifically, as the anomalous, anticyclonic wind stress curl forcing intensifies over the western North Pacific Ocean in 2003–06 (recall Fig. 10a), it causes deepening of the permanent pycnocline and results in vertical spreading

[2] According to the acceleration potential maps in Figs. 11a and b, the meridional velocity due to the mean circulation in the 18°–30°N band is about −0.68 and −0.49 cm s^{-1}, respectively. The meridional velocity due to eddy motions on the STMW isopycnal surface, according to Nishikawa et al. (2010; their Fig. 9c), is <-0.5 cm s^{-1} on average in the 18°–30°N band, and a smaller eddy meridional velocity can be expected on the CMW isopycnal surface. In other words, the maximum combined meridional velocity on the STMW and CMW isopycnal surface is −1.18 and −0.99 cm s^{-1}, respectively, in the 18°–30°N band.

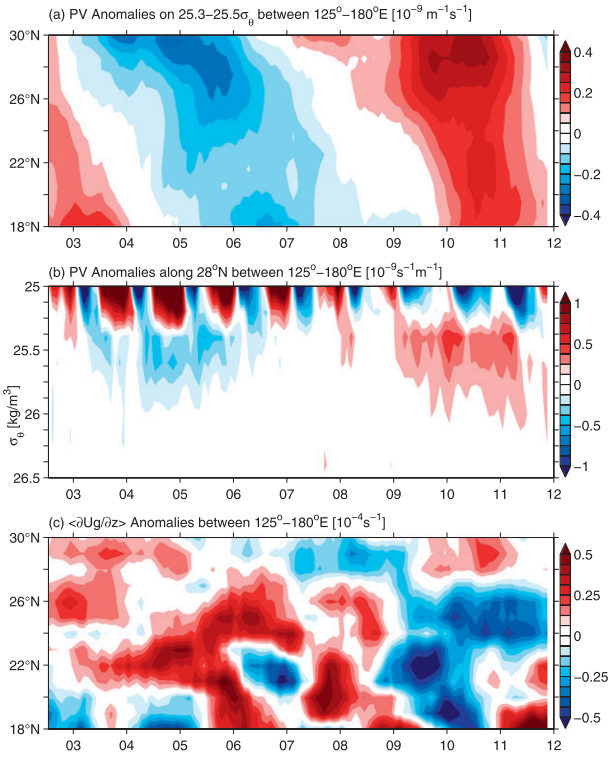

FIG. 12. (a) The PV anomalies averaged zonally from 125°E to 180° on the (25.3–25.5) σ_θ surface of STMW as a function of time and latitude. (b) The PV anomalies averaged zonally from 125°E to 180° along 28°N as a function of time and σ_θ. (c) The $\langle \partial U_g/\partial z \rangle$ anomalies averaged zonally from 125°E to 180° in the surface 150 m layer as a function of time and latitude.

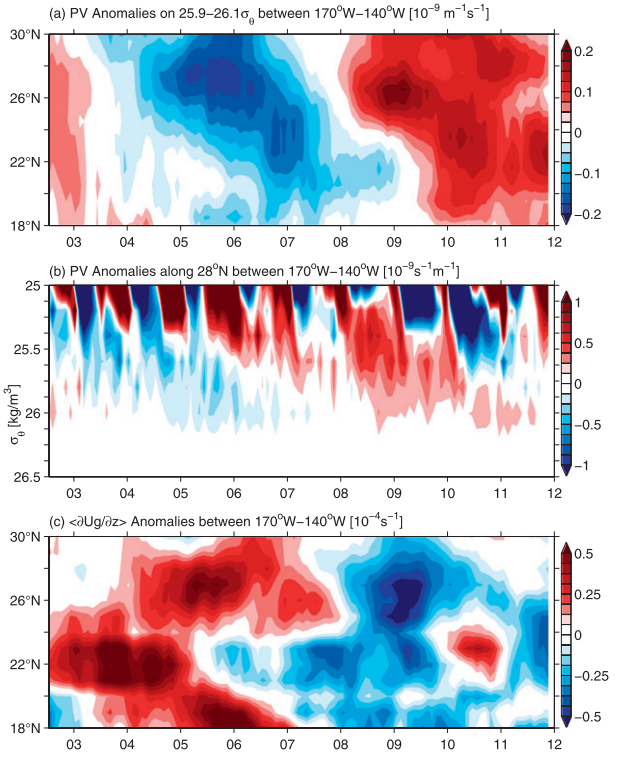

FIG. 13. As in Fig. 12, but for the PV and $\langle \partial U_g/\partial z \rangle$ anomalies averaged zonally from 170° to 140°W. The PV anomalies in (a) are on the (25.9–26.1) σ_θ surface of CMW.

of all isopycnals between the mixed layer and the permanent pycnocline (see Figs. 12b and 13b for the zonally averaged PV anomalies along 28°N as a function of time and σ_θ). In other words, the negative differential PV anomalies seen in Fig. 11 are *not* unique to the STMW and CMW isopycnal surfaces. They appear vertically coherently throughout the wind-impacted isopycnals in the western North Pacific subtropical gyre.

To clarify the relationship between the decadal subsurface PV anomalies and the upper-ocean eastward shear signals, we plot in Figs. 12c and 13c the $\langle \partial U_g/\partial z \rangle$ anomalies averaged zonally in the same manner as in Figs. 12a and 13a. A comparison between the corresponding anomaly patterns reveals that while there exists an overall anticorrelation between the two anomalies, the $\langle \partial U_g/\partial z \rangle$ signals in Figs. 12c and 13c have a tendency to lead the oppositely signed PV signals in Figs. 12a and 13c, respectively. This leading tendency is confirmed in Fig. 14 in which we plot the lag correlation coefficients between the $\langle \partial U_g/\partial z \rangle$ and the PV anomalies averaged in the 18°–30°N band on the STMW and CMW isopycnal surfaces, respectively. In both cases, the maximum correlation is found when the surface eastward shear signals lead the subsurface PV signals by 9 and 15 months. This result of lag correlation is difficult to reconcile if one attempts to attribute the $\langle \partial U_g/\partial z \rangle$ changes to the subsurface PV changes. It is, however, readily understandable when we regard the $\langle \partial U_g/\partial z \rangle$ anomalies as being induced by the surface wind and heat flux forcing and that the subsurface PV anomalies are generated by the same surface wind forcing with the 9- and 15-month lags reflecting the times required, respectively, for the shallow STMW and deep CMW isopycnals to adjust baroclinically.

6. Discussion and summary

Using the available satellite altimeter data of the past two decades, we have explored in this study the decadal mesoscale eddy variability in the southern subtropical gyre (i.e., the 18°–28°N band) of the western North Pacific Ocean. The surface zonal velocity shear in this latitudinal band is largely eastward, and when coupled with the wind-driven westward-flowing North Equatorial Current in the subsurface layer, this vertically sheared system is baroclinically unstable and is the source for the enhanced eddy kinetic energy in the

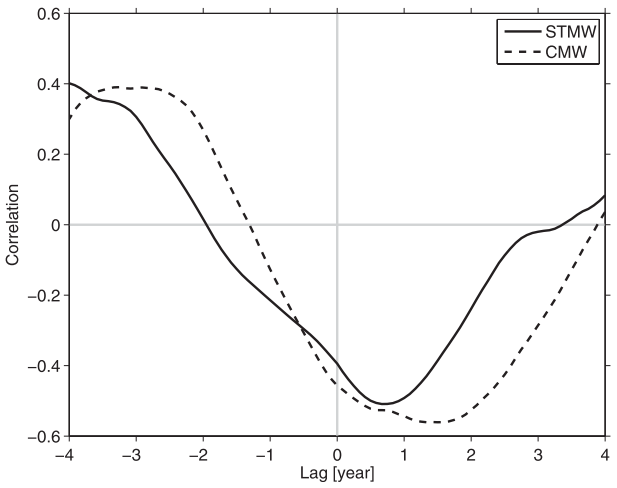

FIG. 14. Lagged correlation between the $\langle \partial U_g/\partial z \rangle$ and PV anomalies in Figs. 12a and 12c (solid line) and between those in Figs. 13a and 13c (dashed line). Here, the lagged correlation is estimated first along each latitude and then averaged within the 18°–30°N band. A positive lag denotes the lead by the $\langle \partial U_g/\partial z \rangle$ signals.

region. By both conducting an EOF analysis and examining the EKE signals in the four quasi-permanent STCC–HLCC bands, we found that the eddy variability is to a large extent spatially coherent and modulates on the decadal time scales. Enhanced eddy activities are detected in 1995–98 and 2003–06, whereas below-average eddy activities are observed in 1999–2002 and 2009–11. In comparison with the local mean EKE level at ~(200–300) $cm^2\ s^{-2}$, the amplitude of the decadal EKE signals can reach ±~(100–150) $cm^2\ s^{-2}$.

Several previous studies have attempted to relate the low-frequency EKE signals in different parts of the STCC band to the Pacific Ocean climate indices. For example, Qiu and Chen (2010) have connected the EKE variability in the northern/southern STCC band to the negative Western Pacific (−WP) index defined by Wallace and Gutzler (1981). Chen and Qiu (2010) and Yoshida et al. (2011), on the other hand, have noted the correlation of the EKE signals in the eastern STCC and HLCC band with the PDO index, respectively. More recently, Chang and Oey (2012) have introduced a Philippines–Taiwan Oscillation (PTO) index defined as the difference in wind stress curls between a box off the Philippines (8°–13°N, 130°–155°E) and a box off Taiwan (22°–25°N, 155°–180°E) to represent the STCC eddy variability.

Given the concurrent EKE changes over the entire southern subtropical gyre identified in this study and given the longer EKE time series available now, it is beneficial to clarify the connection of the STCC EKE variability to these previously used indices. In Figs. 15a, 15b, and 15c, we superimpose the PDO, −WP, and PTO time series (black lines) over the decadal STCC EKE time series, respectively. As summarized in Figs. 15d and 15e, the PDO index is highly correlated with the PTO index ($r = 0.88$) with a lead of 3 months and both can represent the STCC EKE changes favorably at a lead time of 6 and 12 months ($r = 0.72$ and 0.78), respectively. With regard to the −WP index in Fig. 15b, although it had a reasonable representation of the low-frequency EKE changes prior to 2007 (the period covered by Qiu and Chen's 2010 study), this correlation has since deteriorated after 2008. As the PDO index is defined by the oceanic state (i.e., SST) in the entire North Pacific north of 20°N, the connection revealed in Fig. 15a indicates that the STCC EKE variability inside the subtropical gyre band represents one aspect of the broad-scale decadal changes embedded in the North Pacific Ocean.

With the upper-ocean eastward shear $\langle \partial U_g/\partial z \rangle$ providing the energy source for the EKE signals, an upper-ocean temperature budget analysis was conducted to assess the extent to which the surface wind stress and heat flux forcing accounted for the observed $\langle \partial U_g/\partial z \rangle$ signals. Based on the monthly MOAA–GPV T–S data and the NCEP–NCAR reanalysis surface forcing data, we found that the decadal $\langle \partial U_g/\partial z \rangle$ changes in the STCC band are largely determined by the y-dependent surface heat flux forcing. Influence due to the convergent Ekman flux forcing is minor. Our budget analysis confirms that the surface heat flux forcing is not only crucial for the seasonal modifications in the STCC–HLCC eastward shear, but also plays a determinant role in their decadal modulations (Kazmin and Rienecker 1996; Yoshida et al. 2011).

Although it plays a minor role in the upper-ocean $\langle \partial U_g/\partial z \rangle$ signals, the PDO-related surface wind stress forcing is important in increasing the regional SSH, or equivalently deepening the permanent pycnocline, in the western subtropical gyre in 2003–06. Because of the vertical spreading of isopycnals, the subsurface PV values were lower in 2003–06 than in 2009–11. While they tend to initiate in the northern latitude of 30°N, the subsurface PV anomalies were observed to emerge in a vertically coherent manner below the mixed layer, and not be confined to the STMW and CMW isopycnal surfaces. In addition, the PV anomalies were found to expand equatorward at a speed faster than the advective speed along the mode water isopycnals. Given that the decadal subsurface PV anomalies lag behind the upper-ocean $\langle \partial U_g/\partial z \rangle$ anomalies and given that the observed decadal $\langle \partial U_g/\partial z \rangle$ signals can be reasonably accounted for by the surface wind stress and heat flux forcing, we

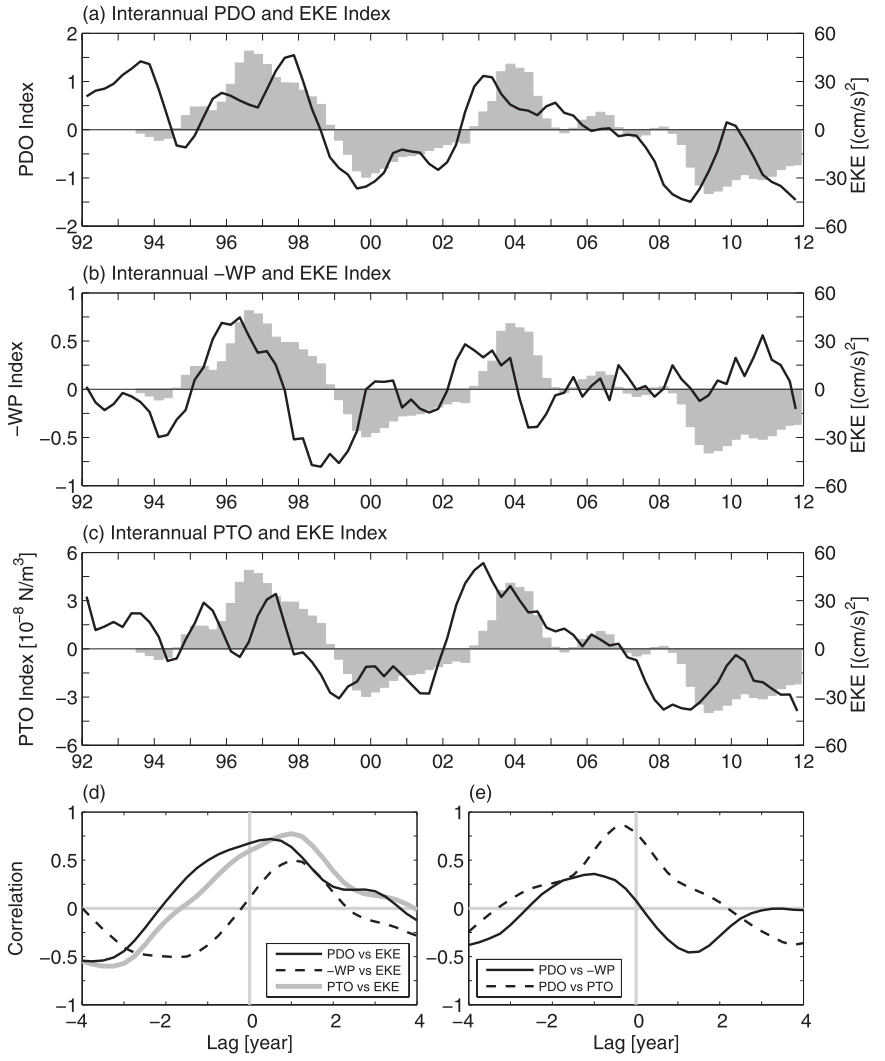

FIG. 15. Time series of (a) PDO, (b) −WP, and (c) PTO indices (solid lines). All three time series have been subjected to an annual running-mean filter. (d) Lag correlation between the decadal EKE time series and the PDO, −WP, and PTO time series. Positive x axis value indicates the lag by the STCC EKE signal. (e) Lag correlation between the PDO and −WP time series and between the PDO and PTO time series. Positive x axis value indicates the lead by the PDO signal.

conclude that for the 2002–11 period analyzed in this study, the subsurface anomalous PV signals did not contribute significantly to the upper-ocean $\langle \partial U_g/\partial z \rangle$ signals that underlie the decadal eddy modulations along the STCC–HLCC band of the western North Pacific subtropical gyre.

With regard to the signals of subsurface PV anomalies, we have in this study relied on the analyses of the MOAA–GPV temperature–salinity data. It would be interesting for future studies to clarify the processes of the PV anomalies' generation, adjustment, and propagation in response to the PDO-related atmospheric forcing.

Acknowledgments. Detailed and constructive comments made by the two anonymous reviewer helped improve an early version of the manuscript. We thank Dr. Shigeki Hosoda of JAMSTEC for providing the monthly MOAA–GPV temperature–salinity data. The surface wind stress and heat flux data were provided by the National Centers for Environmental Prediction and the merged satellite altimeter data by the CLS Space Oceanography Division as part of the Environment and Climate EU ENACT project. This study was supported by NSF through Grant OCE-0926594 and NASA through Contract 1207881 as part of NASA's Ocean Surface Topography Mission.

REFERENCES

Andres, M., J.-H. Park, M. Wimbush, X.-H. Zhu, H. Nakamura, K. Kim, and K.-I. Chang, 2009: Manifestation of the Pacific decadal oscillation in the Kuroshio. *Geophys. Res. Lett.,* **36,** L16602, doi:10.1029/2009GL039216.

Ceballos, L., E. Di Lorenzo, C. D. Hoyos, N. Schneider, and B. Taguchi, 2009: North Pacific Gyre oscillation synchronizes climate variability in the eastern and western boundary current systems. *J. Climate,* **22,** 5163–5174.

Chang, Y.-L., and L.-Y. Oey, 2012: The Philippines–Taiwan Oscillation: Monsoon-like interannual oscillation of the subtropical–tropical western North Pacific wind system and its impact on the ocean. *J. Climate,* **25,** 1597–1618.

Chen, S., and B. Qiu, 2010: Mesoscale eddies northeast of the Hawaiian archipelago from satellite altimeter observations. *J. Geophys. Res.,* **115,** C03016, doi:10.1029/2009JC005698.

Ducet, N., P.-Y. Le Traon, and G. Reverdin, 2000: Global high-resolution mapping of ocean circulation from TOPEX/Poseidon and ERS-1 and -2. *J. Geophys. Res.,* **105,** 19 477–19 498.

Flament, P., S. Kennan, R. Lumpkin, M. Sawyer, and E. Stroup, 1998: The ocean. *Atlas of Hawaii,* S. P. Juvik and J. O. Juvik, Eds., University of Hawaii Press, 82–86.

Hosoda, S., T. Ohira, and T. Nakamura, 2008: A monthly mean dataset of global oceanic temperature and salinity derived from Argo float observations. *JAMSTEC Rep. Res. Dev.,* **8,** 47–59.

Huang, R. X., and B. Qiu, 1994: Three-dimensional structure of the wind-driven circulation in the subtropical North Pacific. *J. Phys. Oceanogr.,* **24,** 1608–1622.

Kazmin, A. S., and M. M. Rienecker, 1996: Variability and frontogenesis in the large-scale oceanic frontal zones. *J. Geophys. Res.,* **101** (C1), 907–921.

Kelly, K. A., R. J. Small, R. M. Samelson, B. Qiu, T. M. Joyce, Y.-O. Kwon, and M. F. Cronin, 2010: Western boundary currents and frontal air–sea interaction: Gulf Stream and Kuroshio Extension. *J. Climate,* **23,** 5644–5667.

Kistler, R., and Coauthors, 2001: The NCEP–NCAR 50-year reanalysis: Monthly means CD-ROM and documentation. *Bull. Amer. Meteor. Soc.,* **82,** 247–267.

Kobashi, F., and H. Kawamura, 2002: Seasonal variation and instability nature of the North Pacific Subtropical Countercurrent and the Hawaiian Lee Countercurrent. *J. Geophys. Res.,* **107,** C03185, doi:10.1029/2001JC001225.

——, and A. Kubokawa, 2012: Review on North Pacific subtropical countercurrents and subtropical fronts: Role of mode waters in ocean circulation and climate. *J. Oceanogr.,* **68,** 113–126.

——, and S.-P. Xie, 2012: Interannual variability of the North Pacific subtropical countercurrent: Role of local ocean-atmosphere interaction. *J. Oceanogr.,* **68,** 21–43.

——, H. Mitsudera, and S.-P. Xie, 2006: Three subtropical fronts in the North Pacific: Observational evidence for mode water-induced subsurface frontogenesis. *J. Geophys. Res.,* **111,** C09033, doi:10.1029/2006JC003479.

Mantua, N. J., S. R. Hare, Y. Zhang, J. M. Wallace, and R. C. Francis, 1997: A Pacific interdecadal climate oscillation with impacts on salmon production. *Bull. Amer. Meteor. Soc.,* **78,** 1069–1079.

Nakamura, H., and A. S. Kazmin, 2003: Decadal changes in the North Pacific oceanic frontal zones as revealed in ship and satellite observations. *J. Geophys. Res.,* **108,** C03078, doi:10.1029/1999JC000085.

Nakano, H., and I. Ishikawa, 2010: Meridional shift of the Kuroshio Extension induced by response of recirculation gyre to decadal wind variations. *Deep-Sea Res. II,* **57,** 1111–1126.

Nishikawa, S., H. Tsujino, K. Sakamoto, and H. Nakano, 2010: Effects of mesoscale eddies on subduction and distribution of Subtropical Mode Water in an eddy-resolving OGCM of the western North Pacific. *J. Phys. Oceanogr.,* **40,** 1748–1765.

Noh, Y., B. Y. Yim, S. H. You, J. H. Yoon, and B. Qiu, 2007: Seasonal variation of eddy kinetic energy of the North Pacific Subtropical Countercurrent simulated by an eddy-resolving OGCM. *Geophys. Res. Lett.,* **34,** L07601, doi:10.1029/2006GL029130.

Nonaka, M., S.-P. Xie, and H. Sasaki, 2012: Interannual variations in low potential vorticity water and the subtropical countercurrent in an eddy-resolving OGCM. *J. Oceanogr.,* **68,** 139–150.

Oka, E., and B. Qiu, 2012: Progress of North Pacific mode water research in the past decade. *J. Oceanogr.,* **68,** 5–20.

Qiu, B., 1999: Seasonal eddy field modulation of the North Pacific Subtropical Countercurrent: TOPEX/Poseidon observations and theory. *J. Phys. Oceanogr.,* **29,** 2471–2486.

——, 2002: The Kuroshio Extension system: Its large-scale variability and role in the midlatitude ocean-atmosphere interaction. *J. Oceanogr.,* **58,** 57–75.

——, and S. Chen, 2005: Variability of the Kuroshio Extension jet, recirculation gyre and mesoscale eddies on decadal timescales. *J. Phys. Oceanogr.,* **35,** 2090–2103.

——, and ——, 2010: Interannual variability of the North Pacific subtropical countercurrent and its associated mesoscale eddy field. *J. Phys. Oceanogr.,* **40,** 213–225.

——, and ——, 2011: Effect of decadal Kuroshio Extension jet and eddy variability on the modification of North Pacific Intermediate Water. *J. Phys. Oceanogr.,* **41,** 503–515.

——, D. Koh, C. Lumpkin, and P. Flament, 1997: Existence and formation mechanism of the North Hawaiian Ridge Current. *J. Phys. Oceanogr.,* **27,** 431–444.

Rio, M. H., S. Guinehut, and G. Larnicol, 2011: New CNES-CLS09 global mean dynamic topography computed from the combination of GRACE data, altimetry, and in-situ measurements. *J. Geophys. Res.,* **116,** C07018, doi:10.1029/2010JC006505.

Roden, G. I., 1975: On North Pacific temperature, salinity, sound velocity and density fronts and their relation to the wind and energy flux fields. *J. Phys. Oceanogr.,* **5,** 557–571.

Roemmich, D., and J. Gilson, 2001: Eddy transport of heat and thermocline waters in the North Pacific: A key to interannual/decadal climate variability? *J. Phys. Oceanogr.,* **31,** 675–687.

——, and Coauthors, 2009: Argo—Observing the global ocean with profiling floats. *Oceanography (Wash. D.C.),* **22,** 34–43.

Sasaki, H., S.-P. Xie, B. Taguchi, M. Nonaka, S. Hosoda, and Y. Masumoto, 2012: Interannual variations of the Hawaiian Lee Countercurrent induced by potential vorticity variability in the subsurface. *J. Oceanogr.,* **68,** 93–111.

Sugimoto, S., K. Hanawa, T. Yasuda, and G. Yamanaka, 2012: Low-frequency variations of the eastern Subtropical Front in the North Pacific in an eddy-resolving ocean general circulation model: Roles of central mode water in the formation and maintenance. *J. Oceanogr.,* **68,** 521–531.

Taguchi, B., S.-P. Xie, N. Schneider, M. Nonaka, H. Sasaki, and Y. Sasai, 2007: Decadal variability of the Kuroshio Extension. Observations and an eddy-resolving model hindcast. *J. Climate,* **20,** 2357–2377.

Wallace, J. M., and D. S. Gutzler, 1981: Teleconnections in the geopotential height field during the Northern Hemisphere winter. *Mon. Wea. Rev.,* **109,** 784–812.

Xie, S.-P., W. T. Liu, Q. Liu, and M. Nonaka, 2001: Far-reaching effects of the Hawaiian Islands on the Pacific ocean-atmosphere system. *Science,* **292,** 2057–2060.

——, L.-X. Xu, Q. Liu, and F. Kobashi, 2011: Dynamical role of mode-water ventilation in decadal variability in the central subtropical gyre of the North Pacific. *J. Climate,* **24,** 1212–1225.

Yamanaka, G., H. Ishizaki, M. Hirabara, and I. Ishikawa, 2008: Decadal variability of the Subtropical Front of the western North Pacific in an eddy-resolving ocean general circulation model. *J. Geophys. Res.,* **113,** C12027, doi:10.1029/2008JC005002.

Yoshida, S., B. Qiu, and P. Hacker, 2011: Low-frequency eddy modulations in the Hawaiian Lee Countercurrent: Observations and connection to the Pacific Decadal Oscillation. *J. Geophys. Res.,* **116,** C12009, doi:10.1029/2011JC007286.